

AperTO - Archivio Istituzionale Open Access dell'Università di Torino

Stability vs. reactivity: understanding the adsorption properties of $\text{Ni}_3(\text{BTP})_2$ by experimental and computational methods

This is the author's manuscript

Original Citation:

Availability:

This version is available <http://hdl.handle.net/2318/138542> since 2016-08-04T16:19:15Z

Published version:

DOI:10.1039/c3dt32944e

Terms of use:

Open Access

Anyone can freely access the full text of works made available as "Open Access". Works made available under a Creative Commons license can be used according to the terms and conditions of said license. Use of all other works requires consent of the right holder (author or publisher) if not exempted from copyright protection by the applicable law.

(Article begins on next page)

This is the author's final version of the contribution published as:

[Greig C. Shearer, Valentina Colomboc, Sachin Chavana, Elisa Albanese,
Bartolomeo

Civalleri, Angelo Maspero, Silvia Bordiga

Stability vs. Reactivity: Understanding the Adsorption Properties of $\text{Ni}_3(\text{BTP})_2$ by
Experimental and Computational Methods

Dalton Trans., 2013,42, 6450-6458, DOI: 10.1039/C3DT32944E]

The publisher's version is available at:

[<http://pubs.rsc.org/en/content/articlelanding/2013/dt/c3dt32944e#!divAbstract>]

When citing, please refer to the published version.

Link to this full text:

[<http://hdl.handle.net/2318/138542>]

This full text was downloaded from iris-AperTO: <https://iris.unito.it/>

iris-AperTO

University of Turin's Institutional Research Information System and Open Access Institutional
Repository

Stability vs. Reactivity: Understanding the Adsorption Properties of Ni₃(BTP)₂ by Experimental and Computational Methods

Greig C. Shearer^{a,b}, Valentina Colombo^{c,d,e}, Sachin Chavan^{a,b}, Elisa Albanese^a, Bartolomeo Civalieri^a, Angelo Maspero,^d Silvia Bordiga^{a*}

^aDipartimento di Chimica, Università di Torino, NIS Centre of Excellence and INSTM Centre of Reference, via Quareello 15/A, 10135 Torino, Italy

^b(present address) inGAP centre of Research-based Innovation, Department of Chemistry, University of Oslo, Sem Saelandsvei 26, N-0315 Oslo, Norway

^cDepartment of Chemistry, University of California, Berkeley, California 94720, United State

^dDipartimento di Scienza e Alta Tecnologia, Università dell'Insubria, via Valleggio 11, 22100 Como, Italy

^e(present address) Dipartimento di Chimica, Università degli Studi di Milano, via Golgi 19, 20133 Milano, Italy.

Abstract

FTIR spectroscopy and *Ab-initio* molecular modelling have been employed to probe the interaction between CO and Ni₃(BTP)₂, a thermally and chemically stable MOF. A combination of low pressure adsorption isotherms and FTIR spectroscopy has been utilised to study the material for its interaction with CO₂ and H₂.

The experimental results indicate that despite an abundance of Ni²⁺ coordination vacancies in the activated sample, the molecular probes considered in this study do not interact with them. These finding are in alignment with the data obtained by molecular modelling, in which it is shown that the unreactive diamagnetic, low spin state is more stable. Due to the strong N-donor character of the pyrazolate ligands on this material, the electrostatic potential map of the optimized structure does not show any evidence of a positive region typical of open metal sites.

1. Introduction

When compared to their inorganic counterparts in zeolites, the low thermal and chemical stability of MOFs is one of their biggest drawbacks in their potential application as sorbents or catalysts.¹⁻³ In acknowledgement of this problem, it has been theorised that the thermal stability of MOFs is mainly governed by the SBU and the strength of the bond between the inorganic component and the linker.^{4, 5} The thermal stability of MOFs is usually limited to 625-675 K but there exists rare cases in which MOFs have been reported to have thermal stabilities above 775 K.⁴⁻⁸

On the other hand, one of the advantageous structural features which some metal organic frameworks possess is open metal sites. Open metal sites are essentially coordination vacancies on metal cations which are incorporated into the framework. These coordination vacancies have been shown to be strong adsorption sites for strategic gases and have been demonstrated to be active as Lewis acid catalytic sites in various reactions.⁹⁻¹³

Up until the $M_3(\text{BTP})_2$ family (BTP = benzenetripyrazolate, **Figure 1a**, $M = \text{Ni}^{2+}, \text{Cu}^{2+}, \text{Zn}^{2+}, \text{Co}^{2+}$) was recently reported by Long and co-workers, there existed no examples of highly thermally and chemically stable metal organic frameworks which also feature coordination vacancies.⁵ The MOFs in this series were conceptually designed to be highly thermally and chemically stable. By noting trends in the stability of MOFs with similar nitrogen donating linkers, the authors found that those whose linkers had higher pK_a values were more stable. With pyrazole having a higher pK_a (= 19.8) than any other functionality previously used on MOF linkers, they designed their materials around this functionality, using the trigonal linker 1,3,5-tris(1H-pyrazol-4-yl)benzene (H_3BTP , Fig 1a.).

Utilising this linker in solvothermal syntheses in the presence of the aforementioned metal cations afforded a series of four MOFs comprising two different topologies. The isostructural nickel and copper analogues feature coordination vacancies, whereas the cobalt and zinc analogues (also an isostructural pair) do not.⁵ Considering a combination of stability and the presence of open metal sites, the $\text{Ni}_3(\text{BTP})_2$ analogue is the most promising material in the series. It was found to be highly thermally and chemically robust, surviving temperatures of up to 700 K in air as well as two weeks of exposure to boiling aqueous solutions with pH ranging 2-14.⁵

The SBU and structure of $\text{Ni}_3(\text{BTP})_2$ are shown in **Figure 1b** and **1c** respectively:

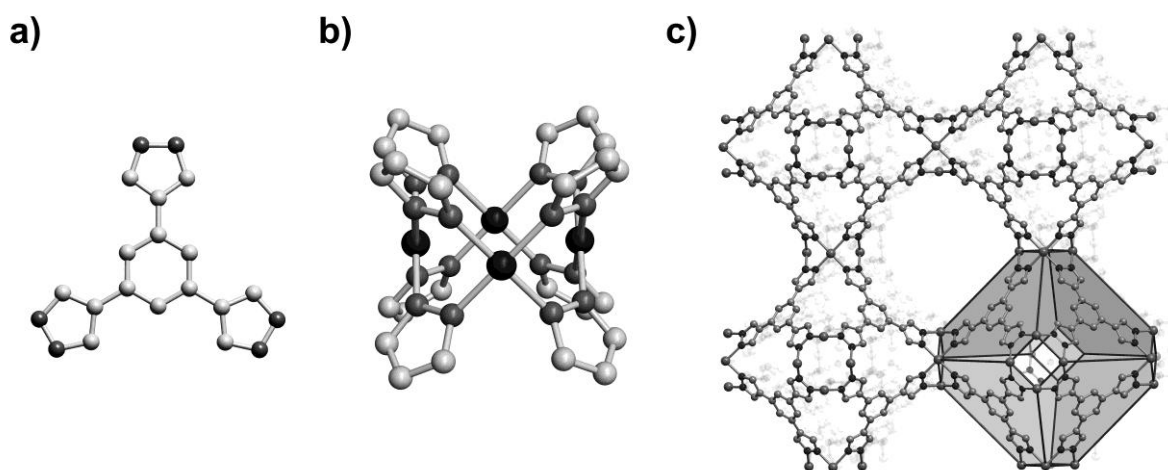


Figure 1:⁵ **a)** Triply deprotonated form of the H_3BTP linker used in the synthesis of the $\text{M}_3(\text{BTP})_2$ series of MOFs; **b)** depiction of the secondary building unit (SBU) of $\text{Ni}_3(\text{BTP})_2$, showing the square-planar Ni_4 cluster bridged by eight exo-bidentate pyrazolate groups; **c)** Structure of $\text{Ni}_3(\text{BTP})_2$ with one of the sodalite cages highlighted. Black, dark grey, and light grey spheres represent Ni^{2+} cations, nitrogen atoms and carbon atoms respectively. Hydrogen atoms are omitted for clarity.

The SBU of this structure consists of four Ni^{2+} cations arranged in square planar geometry. Each bidentate pyrazolate group bridges between two different Ni^{2+} centres so that each SBU stems eight linkers from four square planar coordinated Ni^{2+} cations. The tritopic linkers each bridge between three SBUs to form the overall resulting rigid 3-dimensional structure with sodalite-like octahedral cages, characterized by a high surface area (the BET and Langmuir surface areas are 1650(20) and 1900(13) $\text{m}^2 \text{g}^{-1}$, respectively).⁵

When the material is solvated, Ni^{2+} is in fact in five-coordinate, square pyramidal geometry, with either a methanol, water, or DMF molecule occupying the exposed axial coordination site. The material can be activated to remove these axial ligands, resulting in the exposure of the aforementioned open Ni^{2+} sites, which are directed towards the large channels.⁵

In an attempt to gain insight into the reactivity of these Ni^{2+} coordination vacancies, the present contribution combines experimental and computational studies to elucidate how $\text{Ni}_3(\text{BTP})_2$ interacts with simple probe molecules. The probe molecules were so chosen

because of either their energetic and environmental significance (H_2 and CO_2), or because of their establishment as probes which interact with Lewis acid sites (CO).^{10, 14-17}

It will be shown that even a material with highly favorable properties such as high surface area, thermal and chemical stability and the presence of coordination vacancies is not guaranteed high performance in gas adsorption.

2. Experimental

2.1 Materials and methods

$\text{Ni}_3(\text{BTP})_2$ was made as described in the literature.⁵ For facile activation, the material was post-synthetically methanol exchanged by the method also described in the publication, resulting in the full chemical composition of $\text{Ni}_3(\text{BTP})_2 \cdot 3\text{CH}_3\text{OH} \cdot 10\text{H}_2\text{O}$.⁵

All FTIR spectra were recorded on thin, self-supporting wafers of $\text{Ni}_3(\text{BTP})_2$ produced by the application of ≈ 1 ton of pressure on a pellet press. Porous MOFs are known to have a wide range of hardness values and are particularly prone to structural collapse under sheer stress.¹⁸ Therefore, PXRD was utilised to verify that the material maintains its structural integrity after the pellet pressing (See ESI **Figure S2**). The wafers were subsequently placed in *ad hoc* cells which allowed for thermal treatment in high vacuum (activation), gas dosages, and subsequent *in situ* FTIR measurements. Prior to all *in situ* FTIR measurements, $\text{Ni}_3(\text{BTP})_2$ was activated at 573 K for 16 hours. As this is a higher temperature than the 523 K recommended by Long and coworkers,⁵ checks for structural integrity were implemented by utilising controlled atmosphere capillary PXRD, surface area, pore volume, and pore size distribution measurements. The results of which showed that the material retains its structural integrity after this pre-treatment. (See ESI **Figure S1** and **Table S1**). FTIR experiments performed at ambient temperature were recorded on a Bruker IFS 66 spectrometer in transmission mode at 2 cm^{-1} resolution.

For FTIR measurements in which the temperature was lowered to achieve adsorption (H_2 and CO), the setup had the additional abilities to cool the sample from 300 K down to around 20 K while simultaneously measuring the gas equilibrium pressure. A detailed description of the cryogenic cell (consisting of a modified closed circuit liquid helium Oxford CCC 1204 cryostat) is given elsewhere.¹⁹ In these cases, FTIR spectra were recorded in transmission mode at 1 cm^{-1} resolution on a Bruker Equinox-55 FTIR spectrometer equipped

with an MCT detector and an *ad hoc* modified sample compartment to accommodate the cryogenic IR cell.

Gas adsorption isotherms in pressures ranging from 0-1.1 bar were measured by a volumetric method using a Micromeritics ASAP2020 instrument (Micromeritics Instruments Corp., Norcross, GA). Approximately 100 mg of methanol-exchanged $\text{Ni}_3(\text{BTP})_2$ was transferred to a pre-weighed analysis tube (0.5-inch diameter, 10 cm³ bulb) for evacuation under dynamic vacuum at 525 K. For all isotherms, warm and cold free space correction measurements were performed using ultra-high purity He gas (UHP grade 5.0, 99.999% purity). H_2 isotherms at 77 and 87 K were measured in liquid nitrogen and liquid argon baths, respectively. CO_2 isotherms at 298 K were measured using a Julabo isothermal bath. The H_2 and CO_2 used in these measurements were UHP-grade.

2.2 Computational details

The theoretical investigation of $\text{Ni}_3(\text{BTP})_2$ was carried out with periodic density functional theory (DFT) calculations employing the hybrid B3LYP²⁰ functional augmented with an empirical correction term to include dispersive interactions, as proposed by S. Grimme²¹, with a slight modification for the study of solids.²² Hereafter, the adopted method is denoted as B3LYP-D*. Calculations were performed by using the CRYSTAL09 program,^{23, 24} which has been successfully applied in the study of other MOFs.²⁵⁻²⁷

Crystalline orbitals are represented as linear combinations of Bloch functions (BF), and are evaluated over a regular mesh of points in three-dimensions of reciprocal space. Each BF is built from atom-centered atomic orbitals (AO), which are expressed in terms of Gaussian-type-functions. An all electron basis set has been used for Ni, C, N and H; namely: a modified triple- ζ valence plus polarization (TZVP)²⁸ for Ni, and 6-311G(d,p) for H, C and N. For the numerical integration of the exchange-correlation term, 75 radial points and 974 angular points were adopted in a Lebedev scheme in the region of chemical interest.

The Pack- Monkhorst/Gilat shrinking factors for the k-point sampling of reciprocal space were set to 3 and 6, corresponding to 4 and 20 points at which the Hamiltonian matrix was diagonalized. The accuracy of the integral calculations was increased by setting the tolerances to 7, 7, 7, 7 and 20.

The self-consistent field (SCF) iterative procedure was converged to a tolerance in total energy of $\Delta E = 1 \times 10^{-7}$ a.u.. To accelerate convergence in the SCF process, a modified Broyden's scheme following the method proposed by Johnson was adopted.^{29, 30} The method was applied after ten SCF iterations, with 50% of the Fock/KS matrices mixing and

the Johnson's parameter set to 0.05. The above computational parameters ensured a full numerical convergence on all the computed properties described in this work.

Lattice parameters and atomic positions were fully relaxed until default convergence criteria were satisfied.²³ When considered both alone and in interaction with CO, the point group symmetry of $\text{Ni}_3(\text{BTP})_2$ was kept fixed during the geometric optimization. Adsorption energies have been corrected for BSSE by using the Boys-Bernardi counterpoise correction.³¹ Vibrational frequencies at the Γ point and their IR intensities were calculated on the optimized geometry by means of a mass-weighted Hessian matrix, obtained by numerical differentiation of the analytical first derivatives.^{32, 33}

3. Results and Discussion

3.1 Spectroscopic characterisation of solvent removal

Figure 2 reports the evolution of the FTIR spectra of methanol exchanged sample upon activation under vacuum. In the high frequency range ($3800\text{-}2300\text{ cm}^{-1}$), the spectrum of the as made material is dominated by a broad absorption due to the H-bonded methanol solvent. Upon sample outgassing (from the dot dash black curve to light grey curve), sharp bands above 3000 cm^{-1} due to aromatic $\nu(\text{C-H})$ modes arise. Components below 3000 cm^{-1} evidence traces of residual methanol, in addition to overtones of framework modes. In the low frequency region, the erosion of a band at 1481 cm^{-1} due to the -CH_3 deformation of methanol is observed with increasing activation temperature. Additional components due to the solvent are marked on the figure with asterisks. A detailed description of the framework vibrational modes will be given with the support of animations of computed normal modes (vide infra and in the ESI).

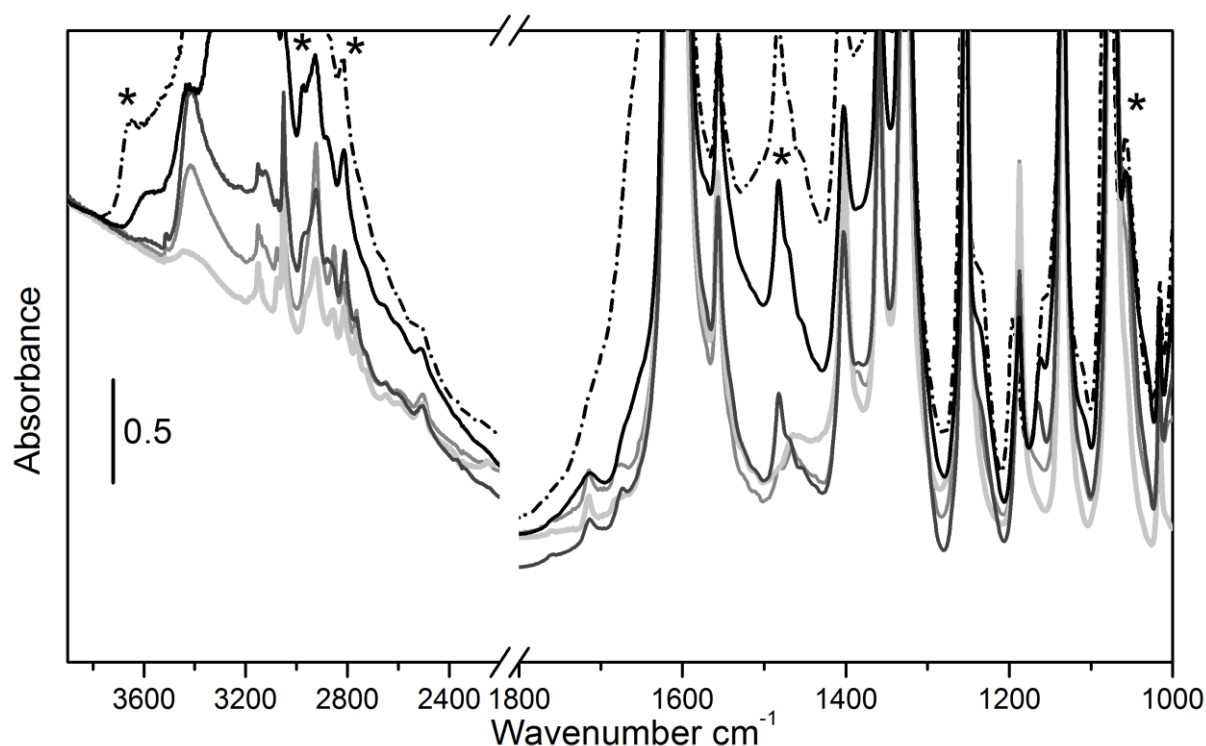


Figure 2: IR spectra of methanol exchanged $\text{Ni}_3(\text{BTP})_2$ (dashed black curve); outgassed for 2 h at RT (black curve); outgassed for 2 h at 473 K (dark grey curve) ; outgassed for 12 h at 523 K (grey curve) outgassed for 12 h at 573 K (light grey curve). Bands marked with asterisks are due to methanol.

3.2 Structure and vibrational properties: experimental and calculated data

3.1.1 Structural Properties

The computed lattice parameters and relevant structural features of both the LS (low spin) and the HS (high spin) configurations of $\text{Ni}_3(\text{BTP})_2$ are listed in **Table 1** and compared with the experimental data obtained by X-ray powder diffraction. The predicted LS phase of $\text{Ni}_3(\text{BTP})_2$ agrees well with the experimentally observed structure with a rather small deviation of 1.6% of the unit cell volume. This shows that $\text{Ni}_3(\text{BTP})_2$ is a diamagnetic material, as would be expected for Ni^{2+} in square planar coordination. This is further confirmed by the higher calculated stability (75 kJ mole^{-1} of Ni atoms) of the LS phase with respect to the HS phase. This rather large difference in energy is a common observation on MOFs with pyrazolate ligands.³⁴ The unit cell volume of the magnetic HS state of $\text{Ni}_3(\text{BTP})_2$ is predicted to be 6.6 % larger Relative to that of the LS state. When CO is adsorbed on the material, the

volume is calculated to be further increased. In each case, the largest structural changes occur at the $\text{Ni}_4(\text{pyrazolate})_8$ SBU of $\text{Ni}_3(\text{BTP})_2$, while the organic linkers show little perturbation.

Table 1. Lattice parameter and unit cell volume of $\text{Ni}_3(\text{BTP})_2$ with and without interaction with CO in the low spin (LS), diamagnetic phase and the high spin (HS), antiferromagnetic configuration^a. Relevant structural features of the square planar Ni_4 cluster linked to the exo-bidentate pyrazolate rings are also reported. ΔE_{stab} is the relative stability of the two phases (HS vs LS) and ΔE_{ads} is the BSSE-corrected interaction energies. Data is presented in Å and kJ mole⁻¹ of Ni atoms.

	Exp	LS	HS ^a	LS/CO	HS/CO ^a
<i>a</i>	18.549	18.650	19.048	18.650	19.112
Volume	6382.1	6486.4	6911.3	6487.0	6980.5
Ni1-Ni2	3.12	3.33	3.51	3.33	3.67
Ni1-Ni3	4.41	4.72	4.97	4.68	5.19
Ni-N	2.02	1.92	2.04	1.91	2.06
Ni ^{···} CO				3.41	2.08
ΔE_{stab}			75.1		30.4
ΔE_{ads}				-6.9	-44.7

^a A pseudo-cubic orthorhombic symmetry is obtained when generating the HS magnetic phase. Accordingly, average values are reported.

Moreover, as shown in **Figure 3**, electrostatic potential mapped on top of the charge density isosurface (i.e. 0.02 au) around the Ni_4 cluster in both the LS (left) and HS (right) magnetic phases, shows peculiar differences. Ni(LS) does not show any evidence of a positive region typical of open metal sites. This result is attributed to the strong N-donor pyrazolate ligands in the Ni^{2+} coordination environment. On the other hand, such a positive region is clearly evident on Ni(HS), indicating a higher propensity for interaction with probe molecules. A negative region is found around the aromatic linker due to the π -electrons. The absence of a positive region typical of open metal sites when in the Ni(LS) form suggests a scarce affinity of the material towards weak Lewis bases such as CO, as is found experimentally in the following section.

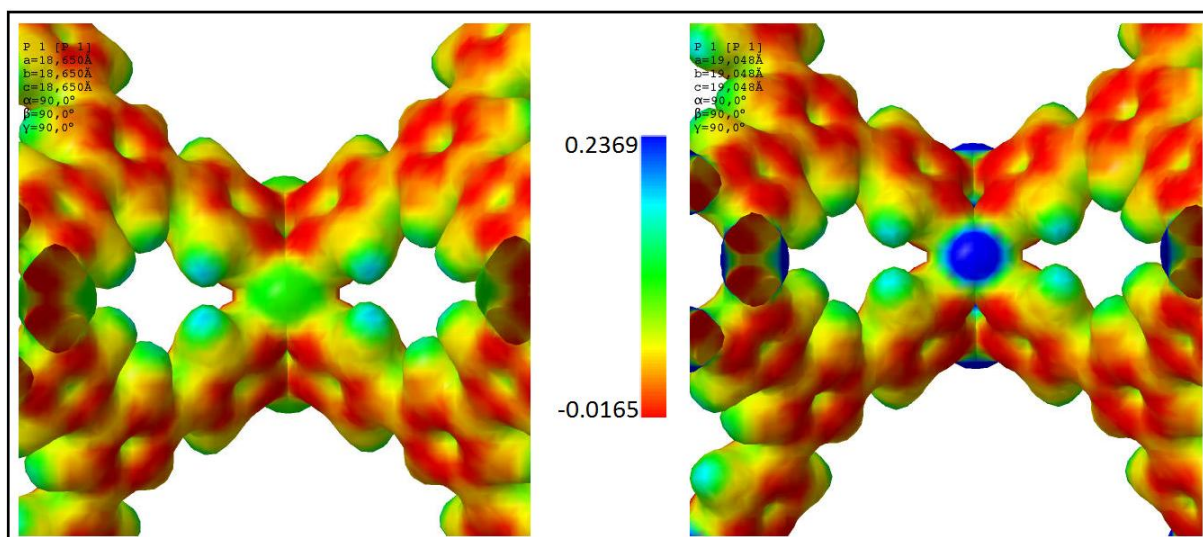


Figure 3: Electrostatic potential (min: -0.0165 a.u, max: 0.2369 a.u.) of the LS (Left) and HS (Right) magnetic phases of $\text{Ni}_3(\text{BTP})_2$ mapped on top of the charge density isosurface (i.e. 0.02 au) around the Ni_4 cluster.

3.1.2 Vibrational Properties

The goodness of fit of the modelling to the data is further confirmed by the comparison between the calculated (black) and experimental (grey) spectra of activated $\text{Ni}_3(\text{BTP})_2$ (in the $1700\text{--}400\text{ cm}^{-1}$ range (**Figure 4**). Note that the calculated frequencies have been scaled by a factor 0.975 (a standard procedure in molecular calculations) to achieve a better agreement with the experimental data.

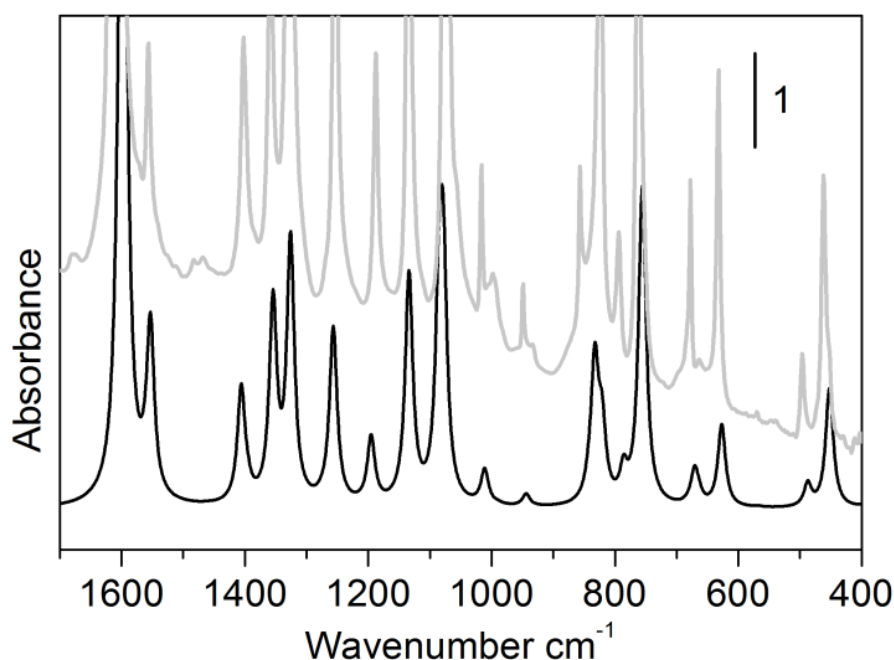


Figure 4: Framework vibrational modes of $\text{Ni}_3(\text{BTP})_2$ in its activated form. Top: experimental spectrum (grey curve), Bottom: theoretical spectrum computed at the Γ point on the optimized geometries, by means of a mass-weighted Hessian matrix obtained by numerical differentiation of the analytical first derivatives. The calculated frequencies are scaled by a factor of 0.975 to best fit the experimental IR spectra. The simulated spectrum has been computed using a Lorentzian function with a FWHM of 15 cm^{-1} .

The excellent agreement between the calculated and experimental $\text{Ni}_3(\text{BTP})_2$ spectrum allows its full assignment by describing the computed vibrational modes which may be observed as animations. By dividing the full range of skeletal modes into sub-ranges, a succinct summary of the spectrum is possible: (i) the $1600\text{--}1200\text{ cm}^{-1}$ region features bands due to C-C, C-N and N-N stretching modes.; (ii) the bands in the $1200\text{--}630\text{ cm}^{-1}$ region are mostly due to C-C-C and N-C-H bending modes as well as in and out of plane C-H bending modes.; (iii) the $500\text{--}400\text{ cm}^{-1}$ region features two fingerprint bands ascribable to Ni-N stretching and bending modes. A full, detailed assignment of the spectrum is given in **Table S2** in the ESI.

4.1 Adsorption properties towards CO

4.1.1 IR spectroscopy

Carbon monoxide has been extensively used as a probe molecule in IR spectroscopic studies of the surface properties of a large variety of systems. This type of study has proven particularly useful in the characterisation of Lewis acidic sites such as the coordination vacancies found on some MOFs.^{17, 35} Two previous studies on the open metal site containing MOFs Ni₂(dhtp), and Cu₃(BTC)₂ (HKUST-1) exemplify the result expected when CO interacts with coordination vacancies in MOFs. In both these studies, with respect to the gas phase value of 2143 cm⁻¹, $\nu(\text{CO})$ was found to blue shift upon adsorption, and by nearly the same value. The main $\nu(\text{CO})$ feature in the spectra of Ni₂(dhtp), and Cu₃(BTC)₂ appear at 2178 and 2179 cm⁻¹ respectively, corresponding to M²⁺...CO adducts.^{17, 35}

A blue shift with respect to gas phase $\nu(\text{CO})$ upon interaction with a transition metal cation can be caused by both M²⁺ \leftarrow CO σ -bonding and by interactions of a purely polarising, electrostatic nature. The magnitude of the shift is indicative of the strength of interaction.³⁶ For example, on the strongest open Ni²⁺ site of the phosphonate MOF Ni-STA-12, $\nu(\text{CO})$ was found to be 2170 cm⁻¹, a significantly lower blue shift than that found on Ni₂(dhtp), and Cu₃(BTC)₂, indicating a weaker adsorbent-adsorbate interaction on this material.³⁷ A significant red shift, on the other hand, indicates that the dominant interaction is of M²⁺ \rightarrow CO π^* -back banding nature. When dealing with transition metal cations, a combination of all three modes of interaction can be expected.³⁶

Figure 5 reports a sequence of IR spectra collected on activated Ni₃(BTP)₂ upon dosing 30 mbar of CO and progressively decreasing the temperature from 200 K to 60 K. The series of spectra show only extensive CO liquefaction inside the pores.

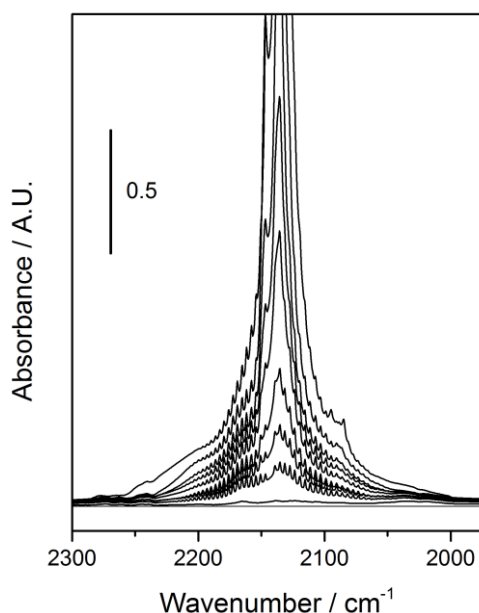


Figure 5: FTIR spectra of the adsorption of 30 mbar CO on $\text{Ni}_3(\text{BTP})_2$ upon cooling from 200 K to 60 K.

The main feature due to adsorbed CO appears at 2136 cm^{-1} , easily ascribed to liquefied CO inside the cavities. The observation of such a small red shift of 7 cm^{-1} with respect to the gas phase allows such an assignment, in correspondence with much previous literature.^{38, 39} Accompanying the main absorption is a shouldering band observed at 2147 cm^{-1} . This high frequency shoulder is commonly observed in similarly assigned spectra, and is assigned as fine structure to the main component, appearing due to the fact that the weakly adsorbed CO molecules act as hindered rotors when placed in an asymmetric environment.³⁹ Also observed in the spectra is a doublet at 2094 and 2084 cm^{-1} at high coverage. This can be assigned in the same way, albeit corresponding to the 1.1 % abundant ^{13}CO and its fine structure. It is clear from the assignment of the spectra that, contrary to what might be expected, CO does not interact with coordinately unsaturated Ni^{2+} sites on this material.

4.1.2 Molecular modelling

In order to explain the experimental results, B3LYP-D* calculations were employed to study the interaction of CO with the Ni²⁺ sites of Ni₃(BTP)₂ in both the LS and HS states. The similarity of the predicted and observed Ni²⁺...CO adsorption energies on Ni₂(dhtp)²⁷ demonstrates the reliability of adsorption energies computed in this way.

The results are reported in **Table 1** and show that the adsorption energies are very different depending on the spin state of the material. In Ni(LS), the interaction is almost negligible (i.e. less than -10 kJmol⁻¹), with the CO molecule keeping a considerable distance from the open metal site, whereas in Ni(HS), the molecule lies closer to the metal atom with a significant adsorption energy of -44.6 kJ mol⁻¹.

This result is in agreement with what is seen in the electrostatic potential maps shown in **Figure 3**, where Ni(LS) is found to be lacking the positive region typical of open metal sites, a feature which is indeed present on Ni(HS). This suggests that only the Ni(HS) state of Ni₃(BTP)₂ will interact strongly with weak Lewis basic probe molecules such as CO.

As was previously discussed, the barrier between the LS and HS states of Ni₃(BTP)₂ is calculated to be about 75 kJ per mole of Ni atoms, and thus the diamagnetic LS structure is adopted by the material. This explains why only a very weak, physisorptive interaction is observed in the experimental data.

However, the fact that Ni₃(BTP)₂ is expected to interact strongly with CO in Ni(HS) suggests that adsorption at the Ni²⁺ sites may be possible if a spin crossover transition can be induced by the application of an external stimulus such as light irradiation. It may therefore be possible for Ni₃(BTP)₂ to be used as a photoswitchable gas storage device. Work is in progress to investigate this possibility.

4.2 Adsorption properties towards CO₂

The FTIR spectra shown in **Figure 6a** depict the gradual spectroscopic changes observed in the region of the CO₂ fundamentals following the desorption of a maximum dose of 12 mbar of CO₂ from a pellet of activated Ni₃(BTP)₂.

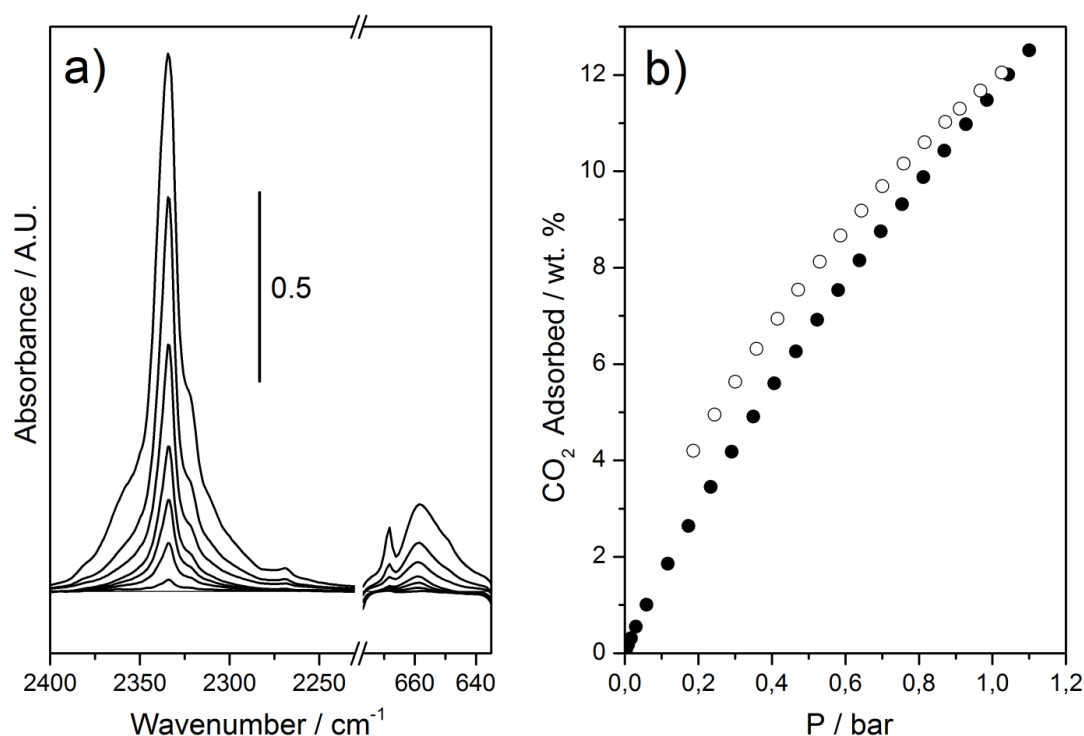


Figure 6 a) FTIR spectra showing the gradual spectroscopic changes observed when following the desorption of 12 mbar of CO₂ from activated Ni₃(BTP)₂. **b)** CO₂ adsorption isotherm measured at 298 K. Filled and empty circles denotes adsorption and desorption, respectively.

Upon adsorption of CO₂ on Ni₃(BTP)₂, bands appear at 2334, 2322, 658, and 668 cm⁻¹. The band at 2334 cm⁻¹ is the main component and can be assigned as the asymmetric stretch (ν_3) of the adsorbed species. The similar behaviour of the nearby band at 2322 cm⁻¹ upon CO₂ desorption allows the conclusion that this band is not indicative of a secondary adsorption site and is simply assigned as the fine structure of weakly adsorbed CO₂. The vibrational frequency of the ν_3 mode is red shifted by 15 cm⁻¹ with respect to molecular CO₂ in the gas

phase. When considering the expected situation in which CO₂ interacts with the Ni²⁺ metal cation through lone pair electron donation from one of its oxygen atoms, usually a blue shift is observed, as in several studies on the CO₂ adsorption at cation sites in zeolites.⁴⁰

A red shift of this band is usually observed in cases in which CO₂ is acting as an electron acceptor through its carbon atom.⁴¹ However, this is not a realistic possibility as a main adsorption site on this material, where the electron donating lone pairs from the pyrazolate group of the linker are already involved in binding to Ni²⁺. Red shifts have also been observed in cases in which there are no specific interactions involved between CO₂ and the adsorbent and the CO₂ is simply weakly physisorbed, as in silicalites and the non-functional metal organic framework, UiO-66, where the CO₂ asymmetric stretching frequencies were observed at 2341 and 2340 cm⁻¹ respectively.^{40, 42} In these studies, the red shift was attributed to the confinement effect that the material pore structure imparts on the molecule, an effect which is absent in the free gas.^{40, 42} A similar assignment is hence made here, with the lower frequency of 2334 cm⁻¹ explained by the greater confinement effect experienced by CO₂ in the small sodalite-like cages.

The observation of two bands in the CO₂ bending (ν_2) region, at 658 and 668 cm⁻¹ could tentatively be assigned to its loss of degeneracy upon adsorption. However, the contour of the bands is not in keeping with such assignments made in the literature.^{14, 43} These bands are instead assigned as the bending modes of gaseous CO₂ (668 cm⁻¹) and the weakly adsorbed species (658 cm⁻¹) respectively. The presence of gas phase CO₂ further demonstrates the weak interaction between CO₂ and the material. As expected with such weakly bound species, all bands assigned to adsorbed CO₂ were fully reversible after 40 minutes of applied vacuum at room temperature.

This result is supplemented by the ambient pressure CO₂ isotherm (**Figure 6b**) obtained by adsorption measurements on activated Ni₃(BTP)₂ at 298 K. The near-linear adsorption profile for CO₂ adsorption is indicative of its low affinity for the Ni²⁺ sites of this framework. At 1 bar, the CO₂ uptake reaches 12.5 wt. % (3.25 mmol/g), a modest value for a metal organic framework, more closely comparable with the weakly interacting MOF-5 (9.2 %) than Ni₂(dhtp) (22.6 %) under similar conditions.^{14, 44} The uptake is however not significantly lower than that previously observed on the tetrazolate-based open metal site containing MOF Fe-BTT,⁴⁵ where the uptake was found to be 13.5 wt% at 1 bar. However, the uptake obtained at this pressure is mainly due to pore filling and is thus mostly dependent on the surface area of the material.

When comparing materials for their strength of interaction with an adsorbate molecule, one must instead look to the initial slope of the isotherms, corresponding to the saturation of the strongest adsorption sites (i.e. coordination vacancies). The initial slope (0-0.1 bar region) of the low pressure CO₂ isotherm of Fe-BTT is significantly larger than that seen on Ni₃(BTP)₂. At 0.1 bar, Fe-BTT has an uptake of 4.8 wt. %, while at the same pressure Ni₃(BTP)₂ has an uptake of just 1.8 wt. %.⁴⁵ This indicates that Ni₃(BTP)₂ does not possess adsorption sites with anywhere near the strength of the strongly polarising Fe²⁺ coordination vacancies present on Fe-BTT.

4.3 Adsorption properties towards H₂

The adsorption of H₂ was performed by dosing activated Ni₃(BTP)₂ with 84 mbar of H₂ at 298 K and progressively cooling the sample to 19 K, at which point the H₂ was allowed time equilibrate with the material before commencing the desorption by heating. The FTIR spectra following the adsorption and desorption of H₂ from Ni₃(BTP)₂ are illustrated in **Figure 7a** and **b** respectively.

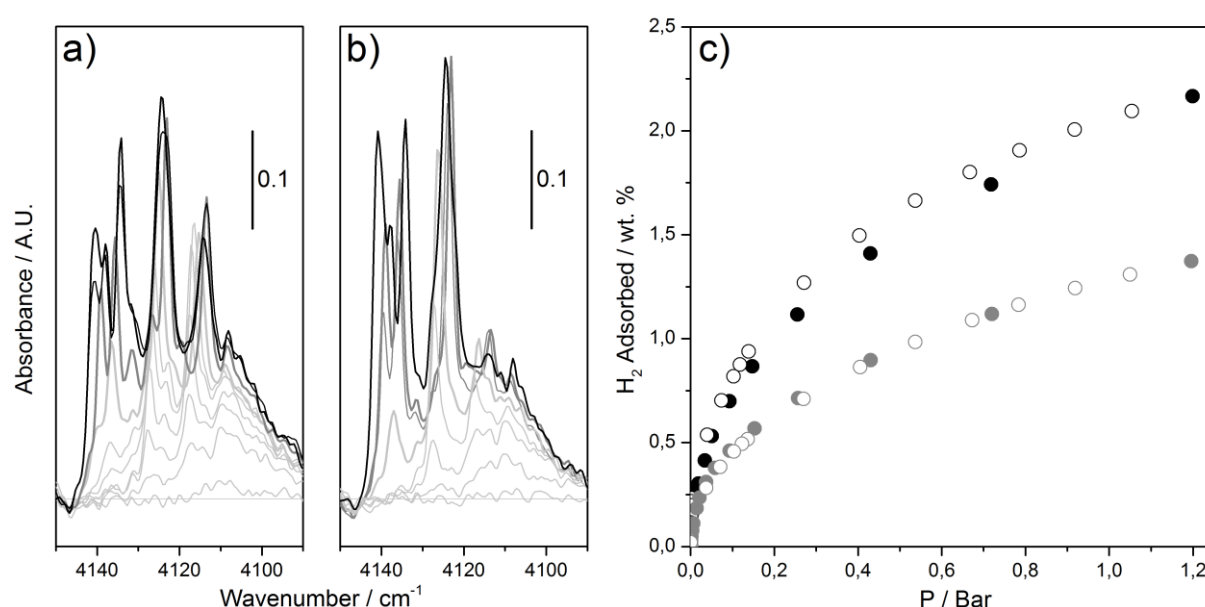


Figure 7: FTIR spectra showing the gradual spectroscopic changes observed on Ni₃(BTP)₂ when following **a)** The adsorption of H₂ by cooling to 19 K and **b)** The desorption of H₂ by heating from 19 K. (H₂ pressure at 298 K and 19 K was 84 and 13 mbar respectively). Shown in Part **c)** are the low-pressure H₂ adsorption isotherms recorded on Ni₃(BTP)₂ at 77 K (black) and 87 K (gray). Adsorption and desorption are represented by filled and hollow symbols, respectively.

The temperature at which a band due to an adsorbed species appears on the spectrum during cooling is known as the onset temperature (T_{onset}). When H_2 is implemented as the probe molecule in VTIR spectroscopic studies on a particular material, the onset temperature has been found to correlate well with its H_2 adsorption enthalpy and is thus a useful parameter to compare between materials.¹⁶

Here, the adsorption onset temperature and pressure as evidenced by FTIR are 95 K and $P_{\text{H}_2} = 32$ mbar, with the first $\nu(\text{H-H})$ bands appearing at 4110 and 4117 cm^{-1} , assigned as the *ortho* and *para* isomers of the initial adsorbed H_2 species respectively. They remain relevant spectral features throughout the adsorption, red shifting to final frequencies of 4109 and 4113 cm^{-1} upon further cooling.

This onset temperature is lower than that observed on most previously studied open metal site containing MOFs.^{16, 46} The fact that the T_{onset} of H_2 on $\text{Ni}_3(\text{BTP})_2$ is 10 K lower than even the open metal site absent MOF-5 is significant, and indicates that the interaction between H_2 and $\text{Ni}_3(\text{BTP})_2$ is very weak and not near the strength observed on the supposedly comparable open Ni^{2+} site containing MOF $\text{Ni}_2(\text{dhtp})$ ($T_{\text{onset}} = 180$ K).¹⁶

Further H_2 adsorption by cooling gives rise to several other bands in the H-H stretching region, evolving with coverage in their own ways until 19 K is reached. After equilibrating for 30 minutes at this temperature, the main component of the spectrum is at 4124 cm^{-1} , with other significant absorptions appearing at 4141, 4138, and 4134 cm^{-1} . Several other minor bands are present at lower frequencies (4120-4100 cm^{-1}), including those which were initially observed on the material, as described above.

During desorption (**Figure 7b**), all bands evolve in the reverse manner to that seen on adsorption, with all H_2 being desorbed at 110 K. A detailed assignment of the bands to their corresponding adsorbed species is beyond the scope of this paper; however the T_{onset} and the shift in the vibrational frequencies of adsorbed H_2 with respect to the gas phase allows us to deduce the strength of the interactions and the likelihood of $\text{H}_2 - \text{Ni}^{2+}$ interactions.

By simply looking at the spectra, their appearance is much more akin to previous studies on the weakly interacting MOF-5 and even porous polystyrene than to those on the open metal site containing HKUST-1 and $\text{Ni}_2(\text{dhtp})$, whose spectra feature only a sharp and defined doublet of high intensity (due to $\text{M}^{2+} - \text{H}_2$ interactions with both *ortho* and *para* H_2) until the metal sites have been saturated at high coverage.^{16, 44, 47}

Closer inspection confirms this observation. Simply considering the H-H vibrational frequencies previously observed on open metal site containing MOFs reveals that the interaction between $\text{Ni}_3(\text{BTP})_2$ and H_2 is not of this kind. When H_2 interacts with an open metal site, $\nu(\text{H-H})$ modes are expected to resonate at a frequency below at least 4100 cm^{-1} . For example, the initial *ortho* and *para* H_2 bands observed on $\text{Ni}_2(\text{dhtp})$ have vibrational frequencies of 4028 and 4035 cm^{-1} respectively. These frequencies are red shifted $\approx 127\text{ cm}^{-1}$ with respect to molecular H_2 , indicating a much larger perturbation of the H-H bond than that on $\text{Ni}_3(\text{BTP})_2$, where the largest red shift observed is 45 cm^{-1} .¹⁶ Moreover, the vibrational frequencies of H_2 adsorbed on $\text{Ni}_3(\text{BTP})_2$ match those on MOF-5 very closely, where bands in the $4110 - 4150\text{ cm}^{-1}$ frequency interval were also seen.⁴⁴

It is therefore concluded, through the analysis of both the T_{onset} and the vibrational frequencies of adsorbed H_2 , that the strength of the interaction between the $\text{Ni}_3(\text{BTP})_2$ is more akin to the weakly interacting MOF-5 or even crystalline nanoporous polystyrene than to that of open metal site containing MOFs such as HKUST-1 and $\text{Ni}_2(\text{dhtp})$, thus indicating that H_2 does not interact with Ni^{2+} coordination vacancies in this material.^{16, 44} Instead, it is suggested that H_2 is simply physisorbed on the walls of the MOF cages, a claim backed by calculations made by Hüber et al. in which it was found that when H_2 interacts with electron rich aromatic systems, $\nu(\text{H-H})$ is expected to be red shifted by $10\text{-}60\text{ cm}^{-1}$ with respect to the Raman frequency of the free molecule.⁴⁸

The low pressure H_2 adsorption isotherms (**Figure 7c**) further support this conclusion. The material exhibits a reversible adsorption (1 bar) of 2.2 and 1.4 wt. % at 77 and 87 K respectively. The uptake obtained at 77 K is nearly identical to those obtained on the azolate-based open metal site containing MOFs Mn-BTT (2.2 wt. %) and Fe-BTT (2.3 wt. %) under the same conditions. However, the uptake obtained at this pressure is mainly due to pore filling and is thus mostly dependent on the surface area of the material.^{45, 49}

In order to elucidate the relative strength of the interaction of H_2 with $\text{Ni}_3(\text{BTP})_2$ with respect to that with Mn-BTT and Fe-BTT, observing the initial slope (0 - 0.1 bar region) of the isotherms again proves useful. The slope observed on the isotherms recorded on Mn-BTT and Fe-BTT are significantly steeper than that recorded on $\text{Ni}_3(\text{BTP})_2$. At 0.1 bar, both Mn-BTT and Fe-BTT achieve a H_2 uptake of 1 wt. %, whereas only 0.7 wt. % is achieved on $\text{Ni}_3(\text{BTP})_2$ at the same pressure. This indicates that the adsorption sites on $\text{Ni}_3(\text{BTP})_2$ are not as strongly polarising as the coordination vacancies present on Fe-BTT and Mn-BTT.

5. Conclusions and Outlook

In situ FTIR spectroscopy measurements have demonstrated that Ni₃(BTP)₂ has poor adsorption properties towards CO, CO₂, and H₂, with the results indicating that all three simply weakly physisorb on the material. The modest uptakes, relatively linear profile, and shallow initial slopes of the low pressure CO₂ and H₂ adsorption isotherms further confirm their low affinity for the material. *Ab-initio* molecular modelling has afforded an explanation for the unexpected result that CO, a strong ligating probe molecule, has such a low affinity towards the Ni²⁺ sites.

Ultimately, the strong pyrazolate ligands force the square planar Ni²⁺ SBU into the low spin, diamagnetic state, with a large LS-HS energy barrier of 75 KJ mol⁻¹. This low spin state is ultimately unreactive and is calculated to have negligible interaction with CO, and is likely to also be the cause of the lack of interaction with the other molecular probes studied.

However, the reactive, high spin state of the material is expected to interact with CO with significant strength (-44.6 KJ mol⁻¹). Adsorption at the Ni²⁺ sites may therefore be possible if a spin crossover transition can be induced by the application of an external stimulus such as light irradiation. It may therefore be possible for Ni₃(BTP)₂ to be used as a photoswitchable gas storage device. Work is in progress to investigate this possibility.

Acknowledgement

Jeffrey R. Long is kindly acknowledged for fruitful discussions. Financial support was provided by "Progetti di Ricerca di Ateneo-Compagnia di San Paolo-2011- Linea 1A" (ORTO11RRT5 project).

6. References

1. G. Ferey, in *From Zeolites to Porous Mof Materials: The 40th Anniversary of International Zeolite Conference, Proceedings of the 15th International Zeolite Conference*, eds. R. Xu, Z. Gao, J. Chen and W. Yan, 2007, vol. 170, pp. 66-84.
2. B. Yilmaz, N. Trukhan and U. Muller, *Chinese Journal of Catalysis*, 2012, **33**, 3-10.
3. U. Mueller, M. Schubert, F. Teich, H. Puetter, K. Schierle-Arndt and J. Pastre, *J. Mater. Chem.*, 2006, **16**, 626-636.
4. J. H. Cavka, S. Jakobsen, U. Olsbye, N. Guillou, C. Lamberti, S. Bordiga and K. P. Lillerud, *J. Am. Chem. Soc.*, 2008, **130**, 13850-13851.
5. V. Colombo, S. Galli, H. J. Choi, G. D. Han, A. Maspero, G. Palmisano, N. Masciocchi and J. R. Long, *Chem. Sci.*, 2011, **2**, 1311-1319.

6. T. Loiseau, C. Serre, C. Huguenard, G. Fink, F. Taulelle, M. Henry, T. Bataille and G. Ferey, *Chem.-Eur. J.*, 2004, **10**, 1373-1382.
7. N. Masciocchi, S. Galli, V. Colombo, A. Maspero, G. Palmisano, B. Seyyedi, C. Lamberti and S. Bordiga, *J. Am. Chem. Soc.*, 2010, **132**, 7902-7904.
8. K. S. Park, Z. Ni, A. P. Cote, J. Y. Choi, R. D. Huang, F. J. Uribe-Romo, H. K. Chae, M. O'Keeffe and O. M. Yaghi, *Proc. Natl. Acad. Sci. U. S. A.*, 2006, **103**, 10186-10191.
9. K. Schlichte, T. Kratzke and S. Kaskel, *Microporous Mesoporous Mat.*, 2004, **73**, 81-88.
10. L. Alaerts, E. Seguin, H. Poelman, F. Thibault-Starzyk, P. A. Jacobs and D. E. De Vos, *Chem.-Eur. J.*, 2006, **12**, 7353-7363.
11. A. Henschel, K. Gedrich, R. Kraehnert and S. Kaskel, *Chem. Commun.*, 2008, 4192-4194.
12. S. Horike, M. Dinca, K. Tamaki and J. R. Long, *J. Am. Chem. Soc.*, 2008, **130**, 5854-5855.
13. D. M. D'Alessandro, B. Smit and J. R. Long, *Angew. Chem.-Int. Edit.*, 2010, **49**, 6058-6082.
14. P. D. C. Dietzel, R. E. Johnsen, H. Fjellvag, S. Bordiga, E. Groppo, S. Chavan and R. Blom, *Chem. Commun.*, 2008, 5125-5127.
15. Z. X. Zhao, Z. Li and Y. S. Lin, *Ind. Eng. Chem. Res.*, 2009, **48**, 10015-10020.
16. J. G. Vitillo, L. Regli, S. Chavan, G. Ricchiardi, G. Spoto, P. D. C. Dietzel, S. Bordiga and A. Zecchina, *J. Am. Chem. Soc.*, 2008, **130**, 8386-8396.
17. S. Chavan, J. G. Vitillo, E. Groppo, F. Bonino, C. Lamberti, P. D. C. Dietzel and S. Bordiga, *J. Phys. Chem. C*, 2009, **113**, 3292-3299.
18. J. C. Tan and A. K. Cheetham, *Chemical Society Reviews*, 2011, **40**, 1059-1080.
19. G. Spoto, E. N. Gribov, G. Ricchiardi, A. Damin, D. Scarano, S. Bordiga, C. Lamberti and A. Zecchina, *Prog. Surf. Sci.*, 2004, **76**, 71-146.
20. A. D. Becke, *J. Chem. Phys.*, 1993, **98**, 5648-5652.
21. S. Grimme, *J. Comput. Chem.*, 2006, **27**, 1787-1799.
22. B. Civalleri, C. M. Zicovich-Wilson, L. Valenzano and P. Ugliengo, *Crystengcomm*, 2008, **10**, 405-410.
23. R. Dovesi, V. R. Saunders, R. Roetti, R. Orlando, C. M. Zicovich-Wilson, F. Pascale, B. Civalleri, K. Doll, N. M. Harrison, I. J. Bush, P. D'Arco and M. Llunell, *CRYSTAL09, University of Torino, Torino*, 2009.
24. R. Dovesi, R. Orlando, B. Civalleri, C. Roetti, V. R. Saunders and C. M. Zicovich-Wilson, *Z. Kristall.*, 2005, **220**, 571-573.
25. B. Civalleri, F. Napoli, Y. Noel, C. Roetti and R. Dovesi, *Crystengcomm*, 2006, **8**, 364-371.
26. A. M. Walker, B. Civalleri, B. Slater, C. Mellot-Draznieks, F. Cora, C. M. Zicovich-Wilson, G. Roman-Perez, J. M. Soler and J. D. Gale, *Angew. Chem.-Int. Edit.*, 2010, **49**, 7501-7503.
27. L. Valenzano, B. Civalleri, K. Sillar and J. Sauer, *J. Phys. Chem. C*, 2011, **115**, 21777-21784.
28. F. Weigend and R. Ahlrichs, *Phys. Chem. Chem. Phys.*, 2005, **7**, 3297-3305.
29. C. G. Broyden, *Math. Comput.*, 1965, **19**, 557-593.
30. D. D. Johnson, *Phys. Rev. B*, 1988, **38**, 12807-12813.
31. S. F. Boys and F. Bernardi, *Mol. Phys.*, 1970, **19**, 553-566.
32. F. Pascale, C. M. Zicovich-Wilson, F. L. Gejo, B. Civalleri, R. Orlando and R. Dovesi, *J. Comput. Chem.*, 2004, **25**, 888-897.
33. C. M. Zicovich-Wilson, F. J. Torres, F. Pascale, L. Valenzano, R. Orlando and R. Dovesi, *J. Comput. Chem.*, 2008, **29**, 2268-2278.
34. E. Albanese, B. Civalleri, M. Ferrabone, F. Bonino, S. Galli, A. Maspero and C. Pettinari, *J. Mater. Chem.*, 2012, **22**, 22592-22602.
35. S. Bordiga, L. Regli, F. Bonino, E. Groppo, C. Lamberti, B. Xiao, P. S. Wheatley, R. E. Morris and A. Zecchina, *Phys. Chem. Chem. Phys.*, 2007, **9**, 2676-2685.

36. C. Lamberti, A. Zecchina, E. Groppo and S. Bordiga, *Chemical Society Reviews*, 2010, **39**, 4951-5001.
37. S. R. Miller, G. M. Pearce, P. A. Wright, F. Bonino, S. Chavan, S. Bordiga, I. Margiolaki, N. Guillou, G. Feerey, S. Bourrelly and P. L. Llewellyn, *J. Am. Chem. Soc.*, 2008, **130**, 15967-15981.
38. S. Bordiga, C. Lamberti, F. Geobaldo, A. Zecchina, G. T. Palomino and C. O. Arean, *Langmuir*, 1995, **11**, 527-533.
39. S. Bordiga, E. E. Platero, C. O. Arean, C. Lamberti and A. Zecchina, *J. Catal.*, 1992, **137**, 179-185.
40. B. Bonelli, B. Civalieri, B. Fubini, P. Ugliengo, C. O. Arean and E. Garrone, *J. Phys. Chem. B*, 2000, **104**, 10978-10988.
41. J. G. Vitillo, M. Savonnet, G. Ricchiardi and S. Bordiga, *ChemSusChem*, 2011, **4**, 1281-1290.
42. M. Kandiah, M. H. Nilsen, S. Usseglio, S. Jakobsen, U. Olsbye, M. Tilset, C. Larabi, E. A. Quadrelli, F. Bonino and K. P. Lillerud, *Chem. Mat.*, 2010, **22**, 6632-6640.
43. A. Vimont, A. Travert, P. Bazin, J. C. Lavalley, M. Daturi, C. Serre, G. Ferey, S. Bourrelly and P. L. Llewellyn, *Chem. Commun.*, 2007, 3291-3293.
44. S. Bordiga, J. G. Vitillo, G. Ricchiardi, L. Regli, D. Cocina, A. Zecchina, B. Arstad, M. Bjorgen, J. Hafizovic and K. P. Lillerud, *J. Phys. Chem. B*, 2005, **109**, 18237-18242.
45. K. Sumida, S. Horike, S. S. Kaye, Z. R. Herm, W. L. Queen, C. M. Brown, F. Grandjean, G. J. Long, A. Dailly and J. R. Long, *Chem. Sci.*, 2010, **1**, 184-191.
46. K. Sumida, D. Stuck, L. Mino, J.-D. Chai, O. Zavorotynska, L. Murray, M. Dinca, S. Chavan, S. Bordiga, M. Head-Gordon and J. Long, *J. Am. Chem. Soc.*, Accepted.
47. S. Figueroa-Gerstenmaier, C. Daniel, G. Milano, G. Guerra, O. Zavorotynska, J. G. Vitillo, A. Zecchina and G. Spoto, *Phys. Chem. Chem. Phys.*, 2010, **12**, 5369-5374.
48. O. Hubner, A. Gloss, M. Fichtner and W. Kloppe, *J. Phys. Chem. A*, 2004, **108**, 3019-3023.
49. M. Dinca, A. Dailly, Y. Liu, C. M. Brown, D. A. Neumann and J. R. Long, *J. Am. Chem. Soc.*, 2006, **128**, 16876-16883.